Supplementary Information

Slow slip modulates low-frequency seismicity on the San Andreas Fault

Zahra Zali[1], Patricia Martínez-Garzón[1,2], David Mencin[3], Gregory C. Beroza[4]

[1] GFZ Helmholtz Centre for Geosciences, Potsdam, Germany

[2] RWTH Aachen University, Aachen, Germany

[3] EarthScope Consortium, Washington DC, U.S.A.

[4] Department of Geophysics, Stanford University, Stanford, California, USA

Correspondence to: Zahra Zali (zali@gfz-potsdam.de)

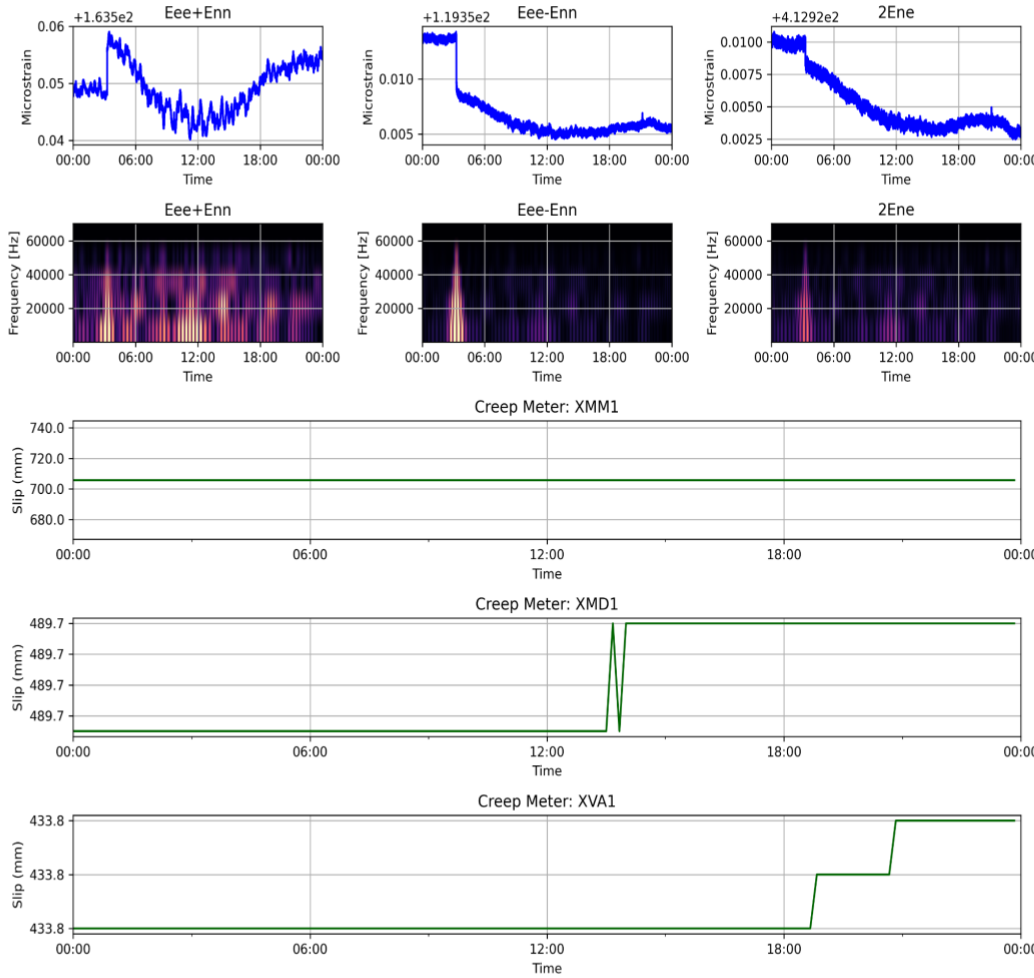

Supplementary Fig. 1: False detection on 2014-07-15 interpreted as non-SSE. Despite a transient in the wavelet transform, the amplitude distribution across components is inconsistent with typical SSE signatures. Specifically, the areal component (Eee+Enn) shows a significantly larger amplitude than the differential and engineering components, suggesting a non-tectonic origin.

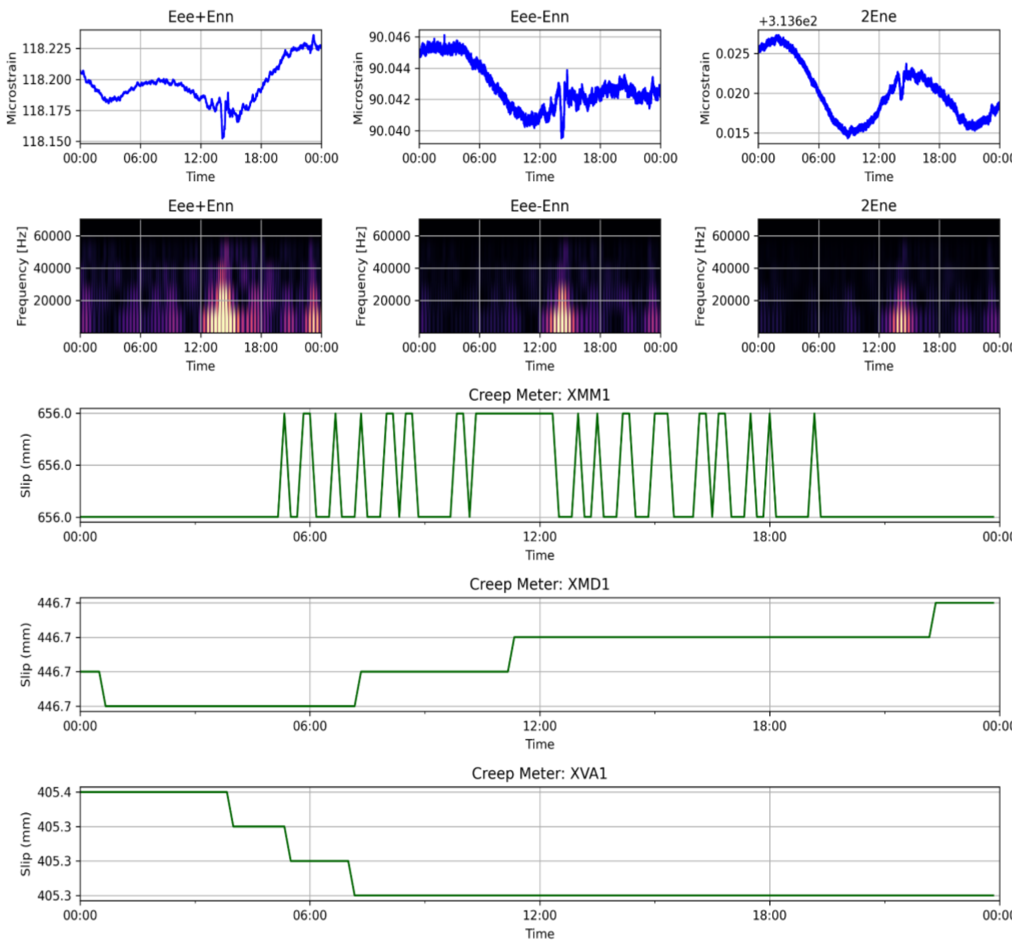

Supplementary Fig. 2: False detection on 2010-11-27 interpreted as non-SSE. The signal exhibits abrupt changes in amplitude but lacks the waveform characteristics of confirmed SSEs.

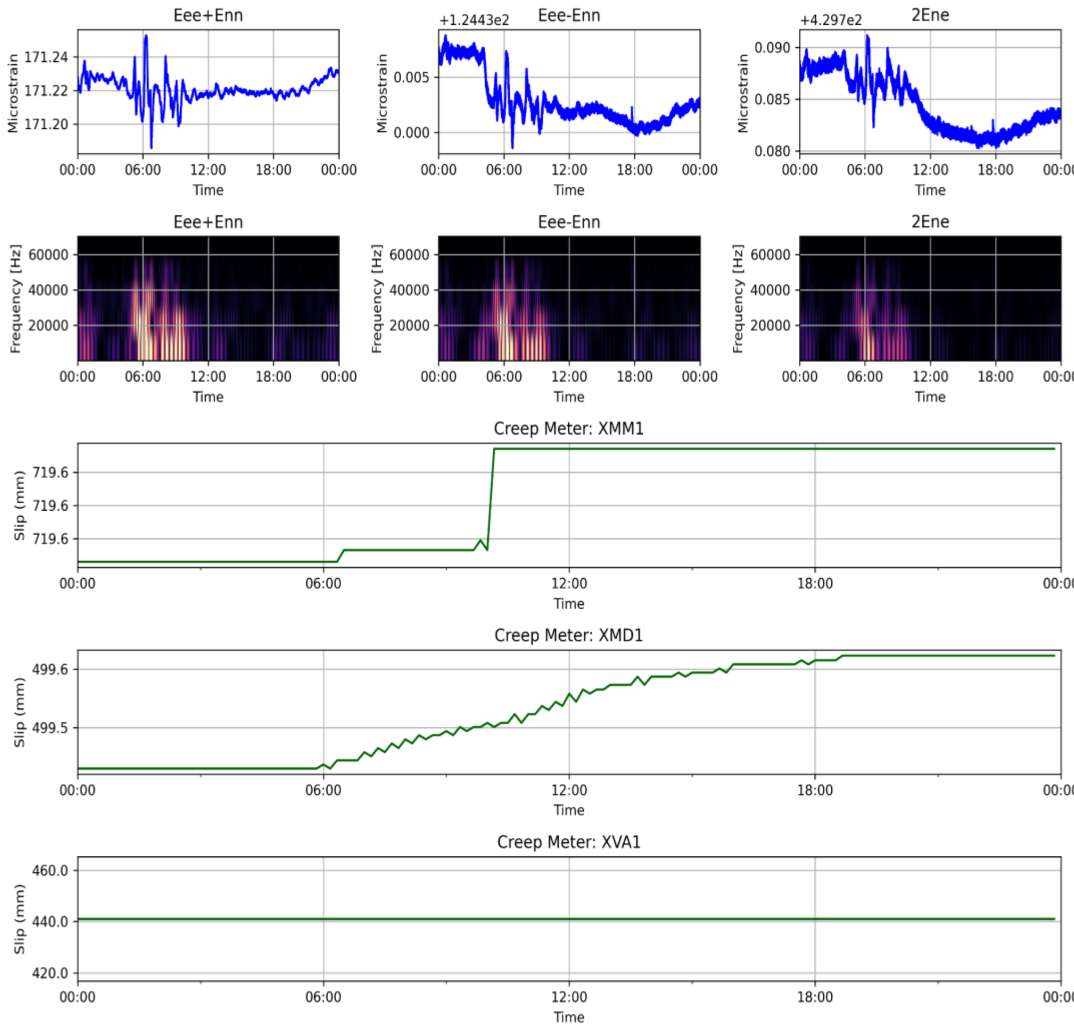

Supplementary Fig. 3: False detection on 2015-10-15 interpreted as non-SSE. Although initially detected by the algorithm, this signal might be attributed to an earthquake.

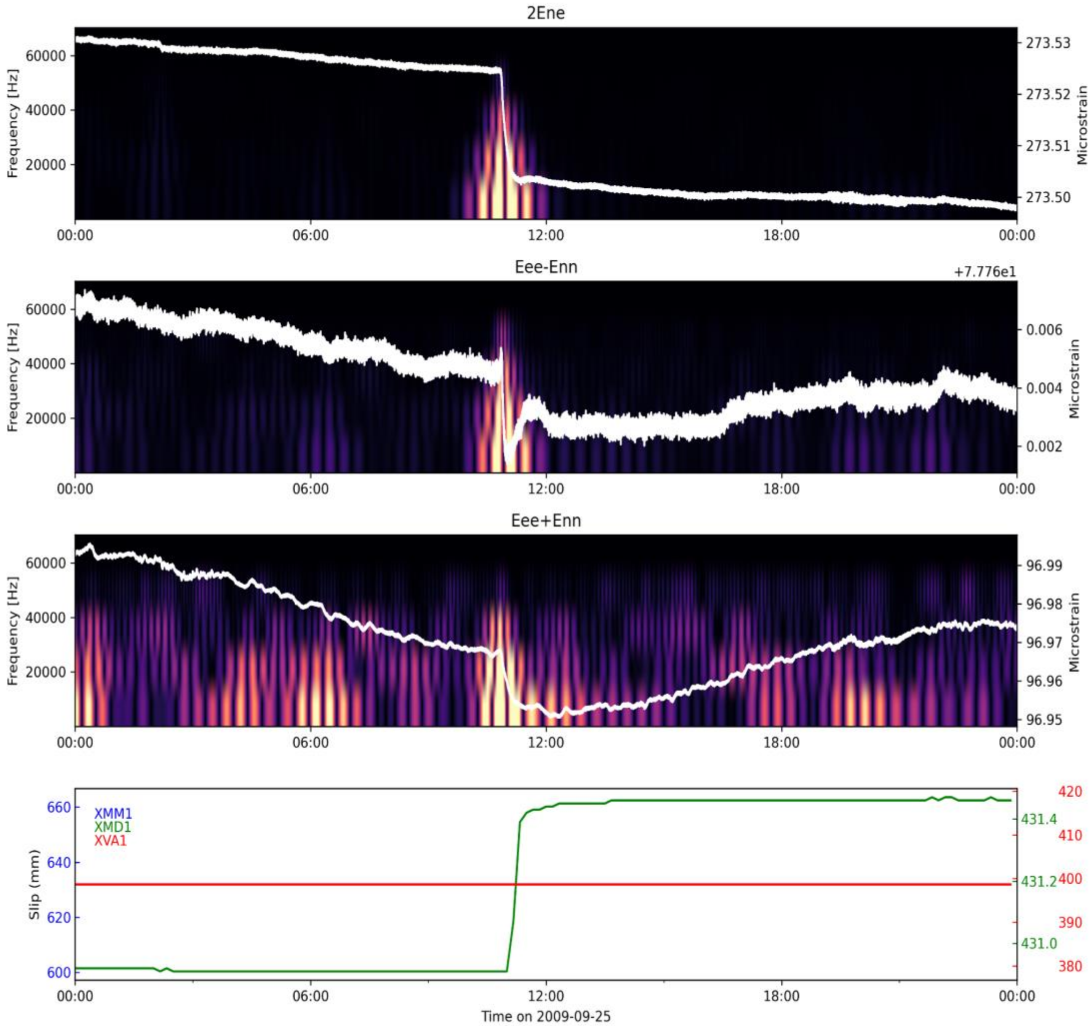

Supplementary Fig. 4: Newly detected SSE not included in the manual catalog. Wavelet transform and strain time series from the three components of strainmeter B073 show a clear transient signal consistent with an SSE, which is also observable on the nearby creepmeter.

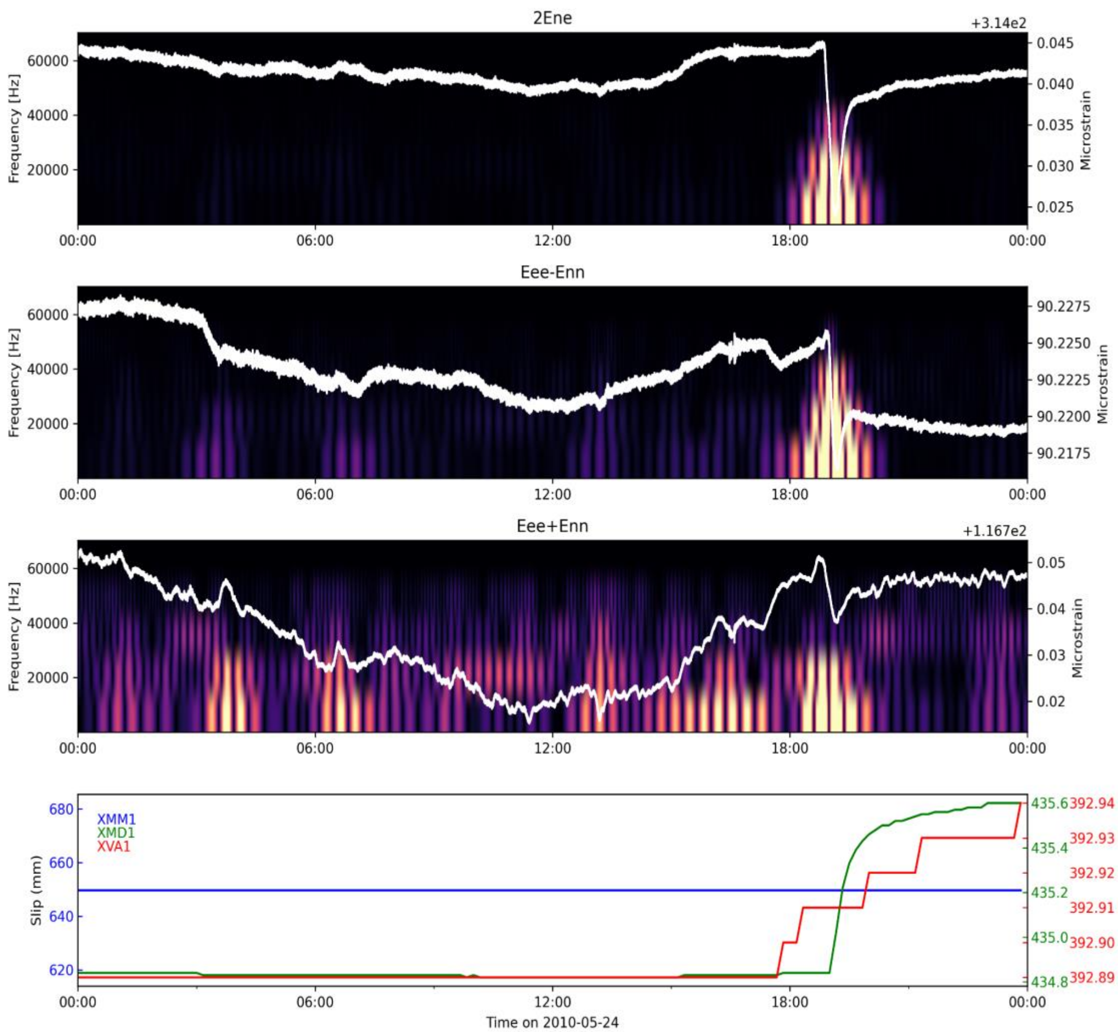

Supplementary Fig. 5: Newly detected SSE confirmed by strain and creepmeter data. Example of an automatically detected SSE supported by coherent signals in the components of B073 and coincident slip on the nearby creepmeter.

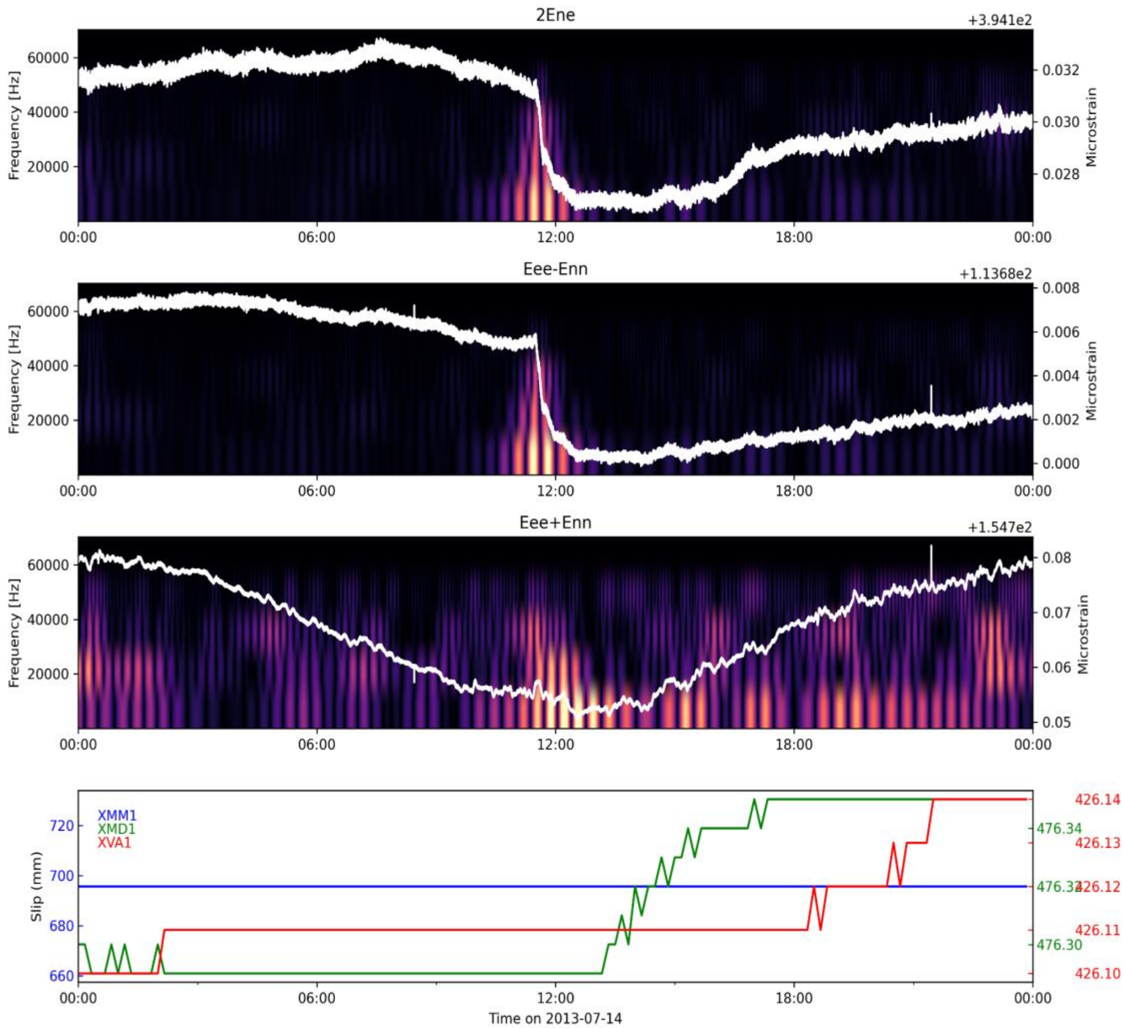

Supplementary Fig. 6: Newly detected SSE with weak expression on creepmeters. Despite the lack of a clear creep signal, the SSE is visible in two components of B073 and confirmed by its waveform and wavelet pattern.

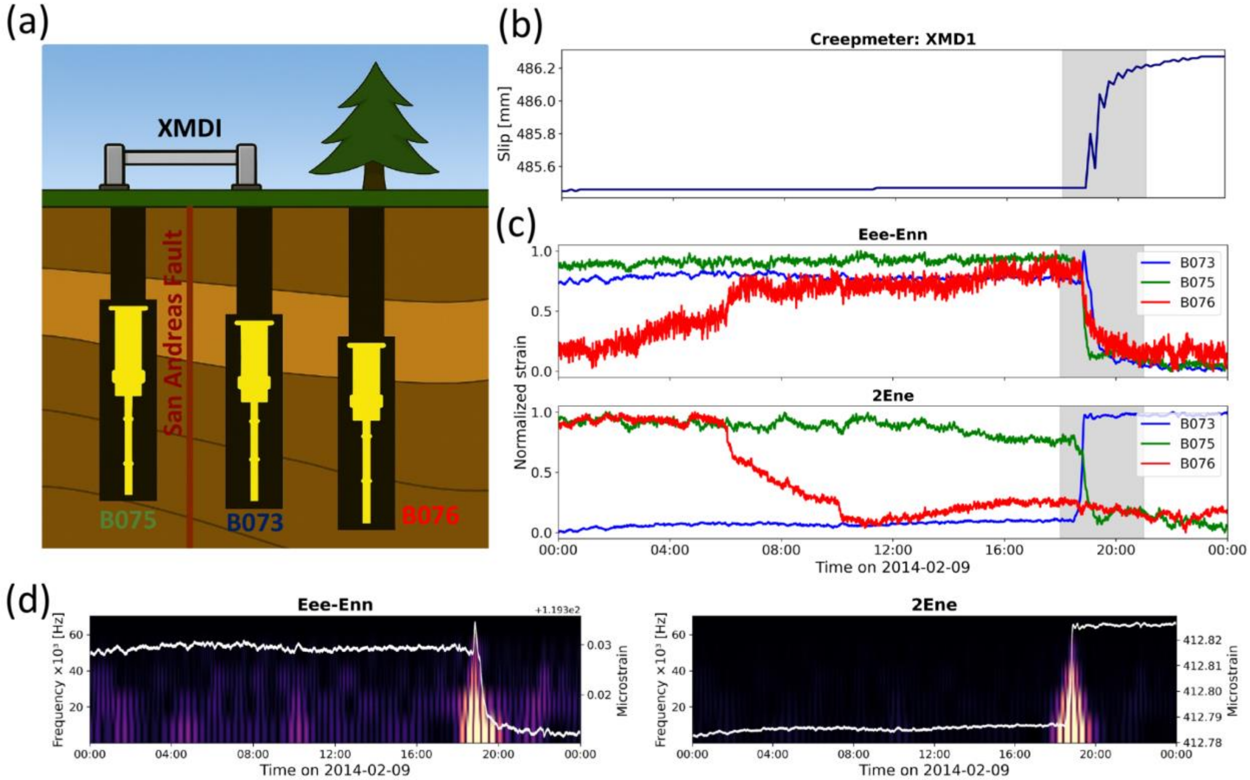

Supplementary Fig. 7: Example of an SSE from the manual catalog also identified by our algorithm. a, Schematic illustration of the instrument configuration, showing the surface creepmeter XMD1 and three borehole strainmeters (B075, B073, B076) installed at ~150 m depth around the San Andreas Fault. **b**, Creepmeter signal indicating surface slip associated with the SSE. **c**, Normalized strainmeter time series from the three strainmeters. The largest strain signal is observed at B073, followed by B075, with the smallest at B076, consistent with their relative positions to the fault. **d,** Daily wavelet transform (WT) of the two strainmeter components. The corresponding strainmeter signals are overlaid in white.

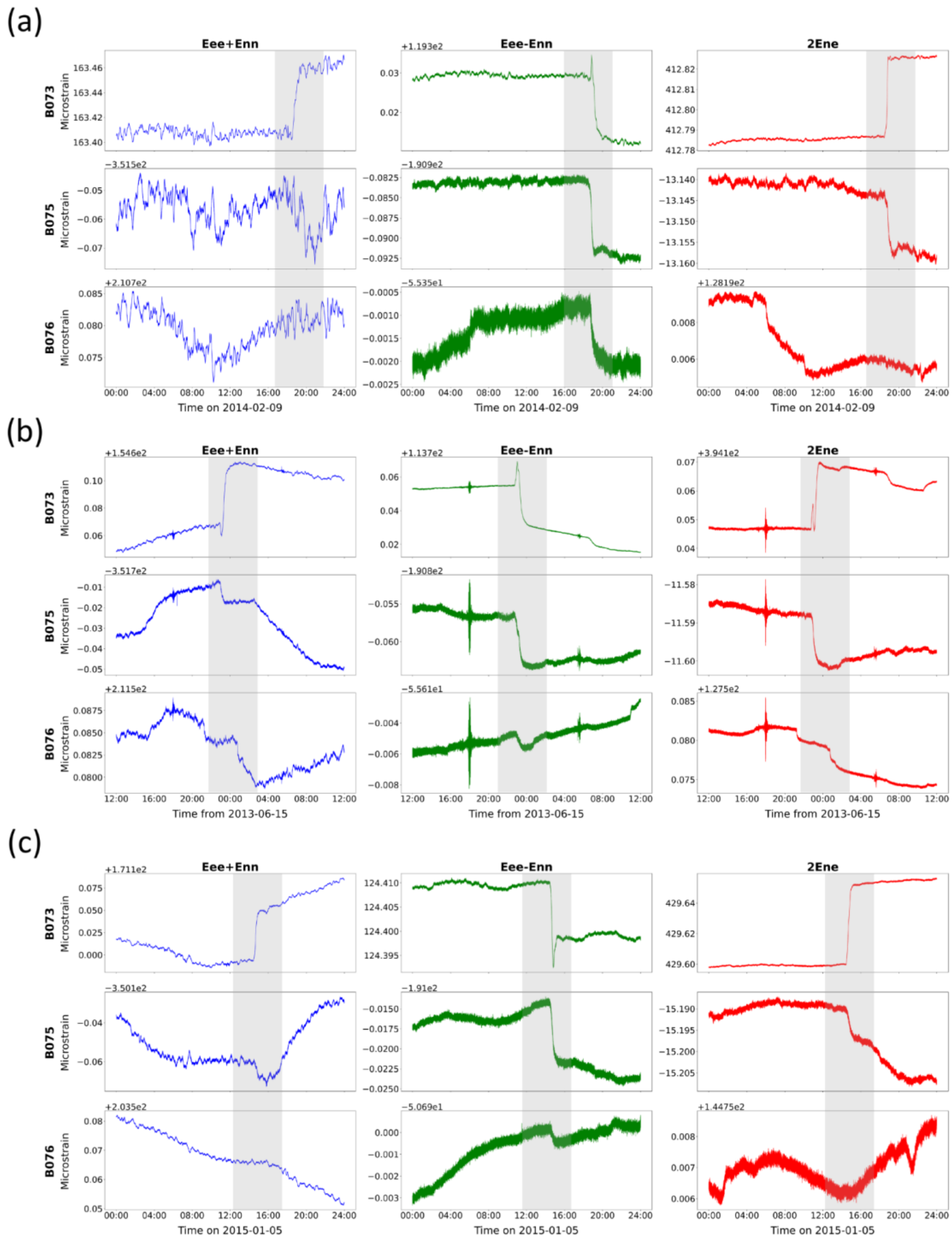

Supplementary Fig. 8: **Examples of SSEs detected on all three strainmeters. a, b, c,** Show strain time series for three different SSEs recorded at stations B073, B075, and B076, respectively. For each station, the areal (Eee+Enn), differential (Eee−Enn), and engineering (2Een) strain components are plotted. The SSEs exhibit consistent transient signals across the stations.

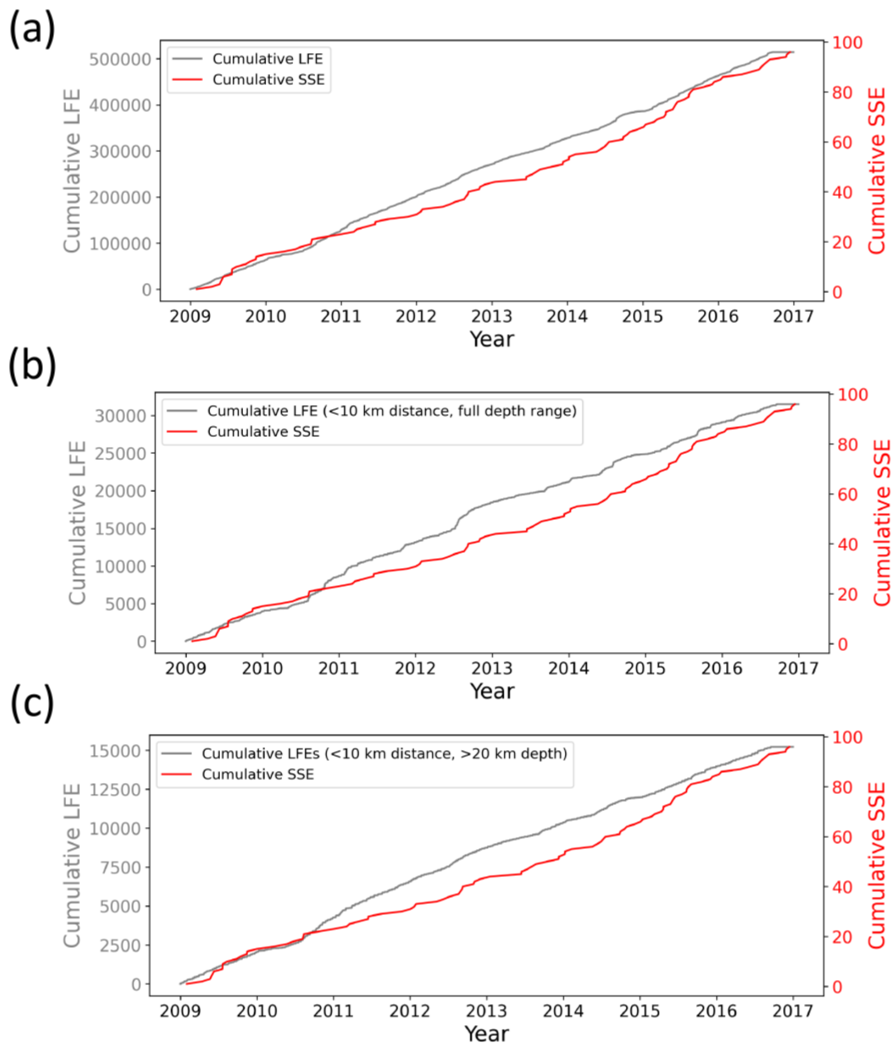

Supplementary Fig. 9: Temporal relationship between SSEs and LFEs. a, Cumulative number of SSEs and LFEs from 2009 to 2016. **b**, Cumulative counts restricted to LFEs within 10 km of station B073. **c**, Cumulative counts restricted to LFEs within 10 km of station B073 and at depths greater than 20 km.

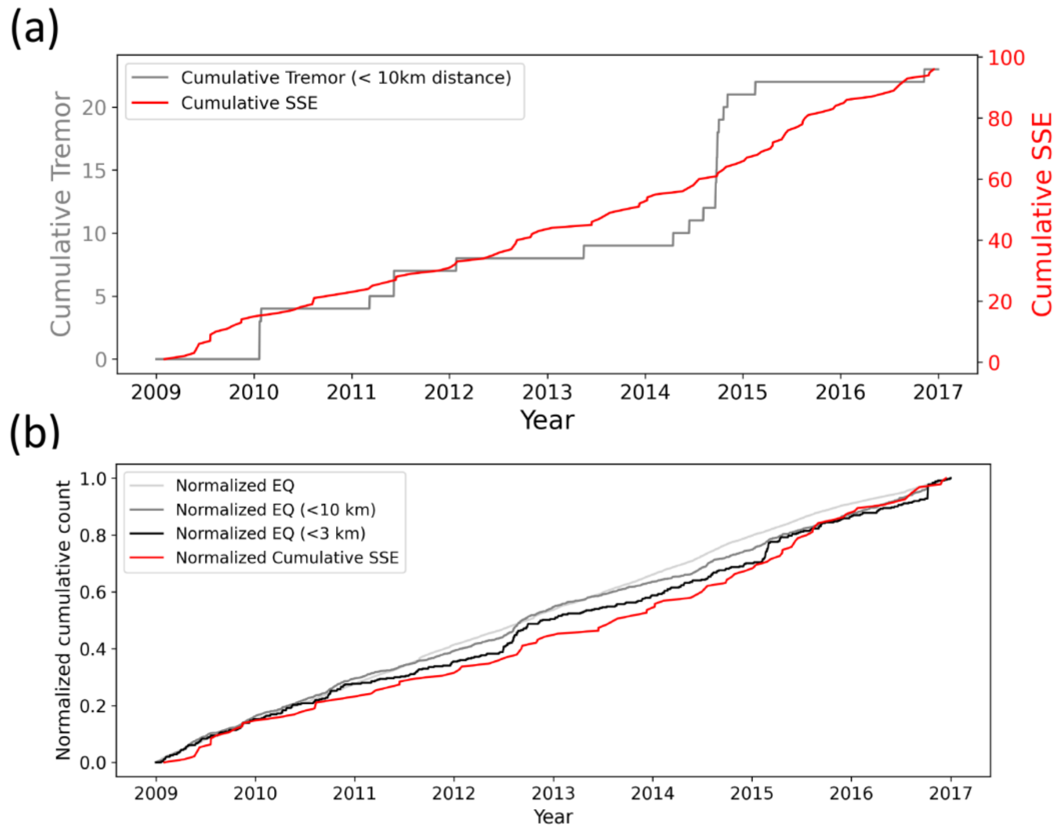

Supplementary Fig. 10: Cumulative number of SSEs with that of earthquakes and tremors. **a,** Cumulative number of SSEs and tremors occurring within 10 km of station B073. No temporal correlation is observed between SSEs and tremor. **b**, Normalized cumulative counts of SSEs and earthquakes for all events in the catalog (light gray), events within 10 km (black), and events within 3 km (dark gray) of B073. A weak correlation is observed between SSEs and 3–10 km earthquakes, but the association is notably weaker than that with LFEs (Fig. 5a). The earthquake catalog is from the Northern California Earthquake Data Center, and the tremor catalog is from the TremorScope catalog (Berkeley Seismology Lab).

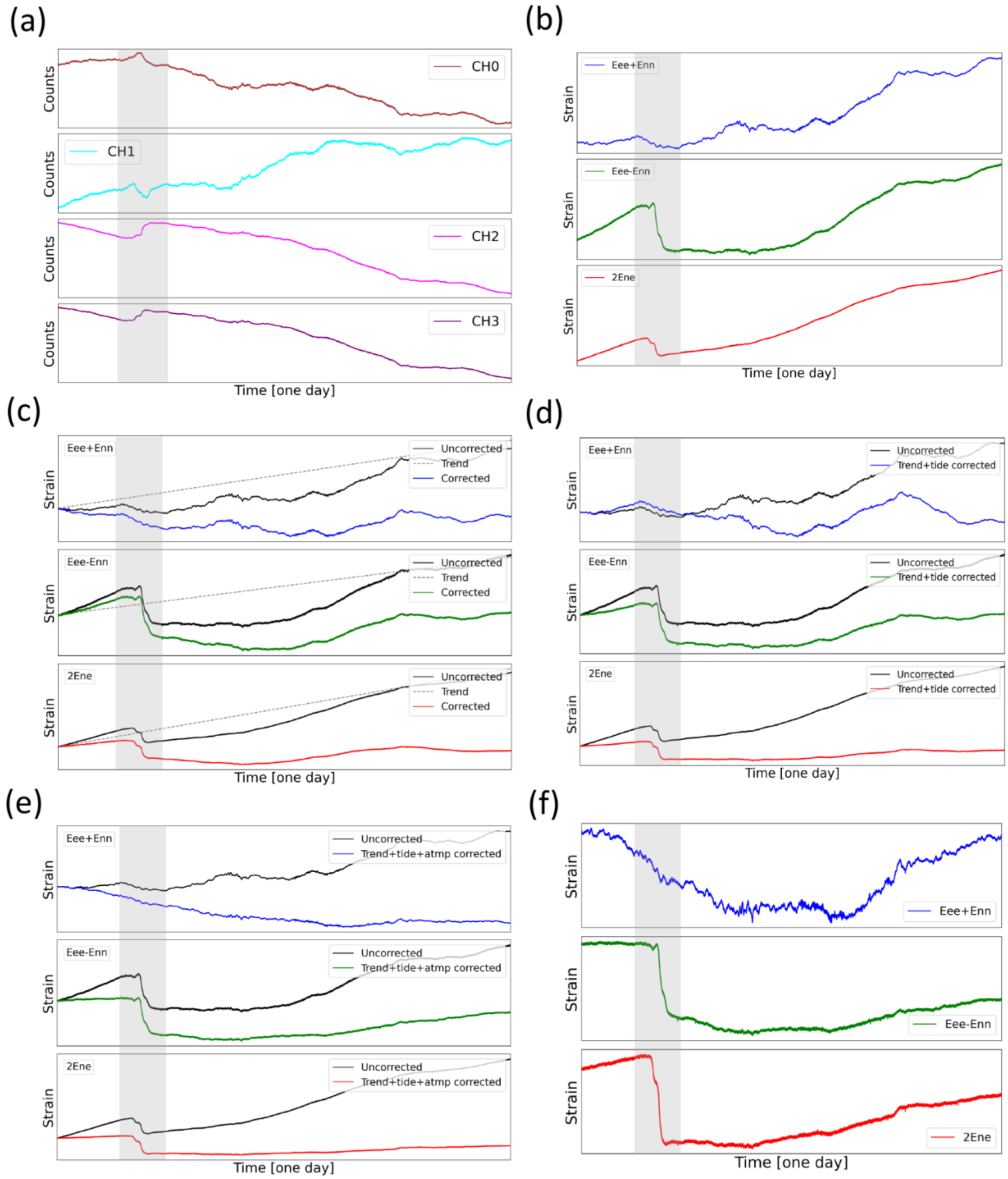

Supplementary Fig. 11: Preprocessing steps for one SSE (on 2009-02-01). a, Raw data from the four gauges of the borehole strainmeter. **b**, Calibration of gauge readings to convert them into strain units. **c-e**, Corrections applied for long-term trend, tidal effects, and atmospheric pressure, respectively. **f**, Final areal, differential, and engineering strain components used for the analysis.

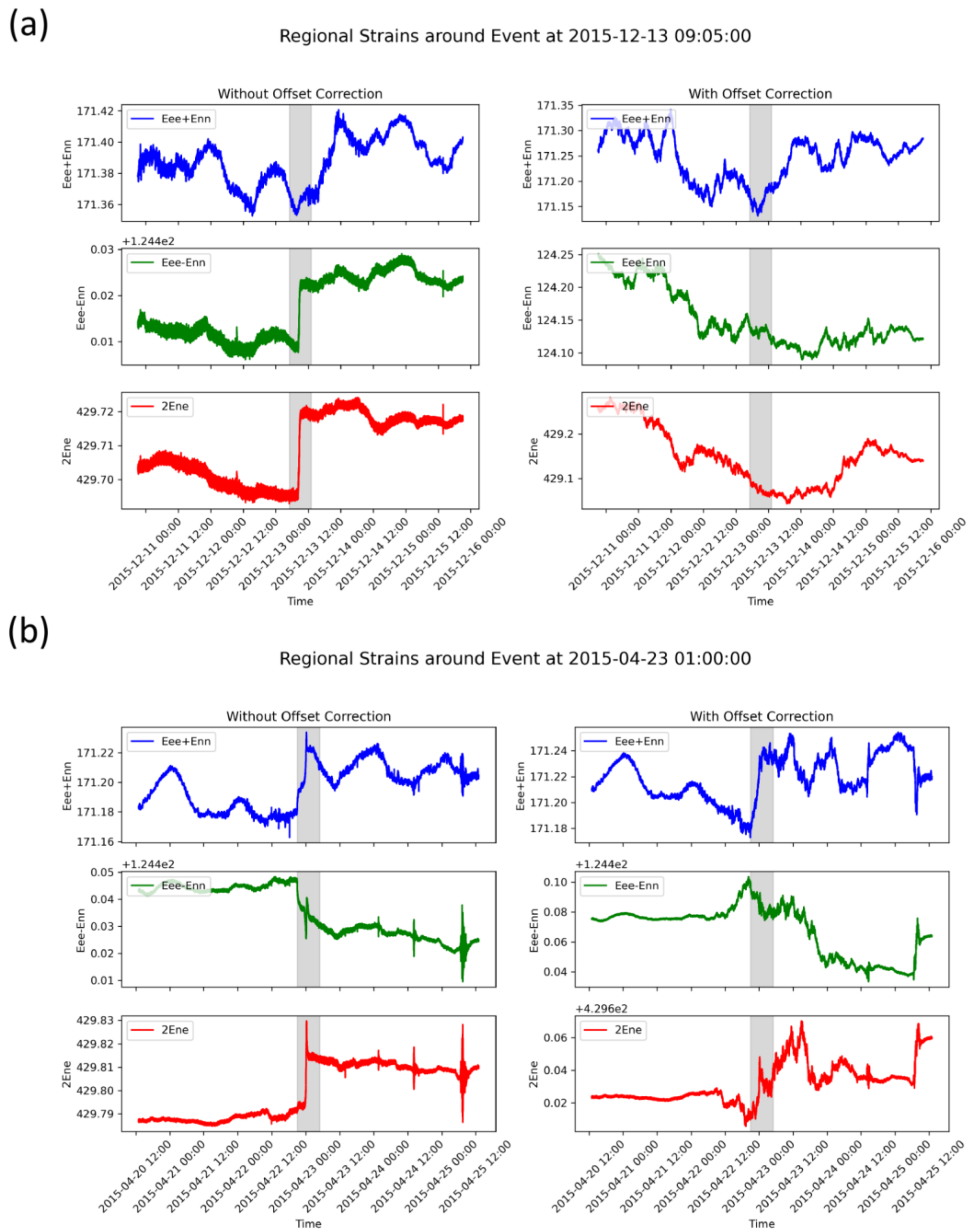

Supplementary Fig. 12: Effect of offset correction on SSE detection. a, and **b,** show two examples of areal (Eee+Enn), differential (Eee−Enn), and engineering (2Een) strain components over a 5-day period, after correction for trend, tidal, and atmospheric pressure effects. The right column shows the original signals, while the left column shows the same data after applying automatic offset correction. In both cases, the SSE signal is distorted or suppressed by the offset correction, potentially leading to failed detection. Therefore, we exclude offset correction from our workflow.

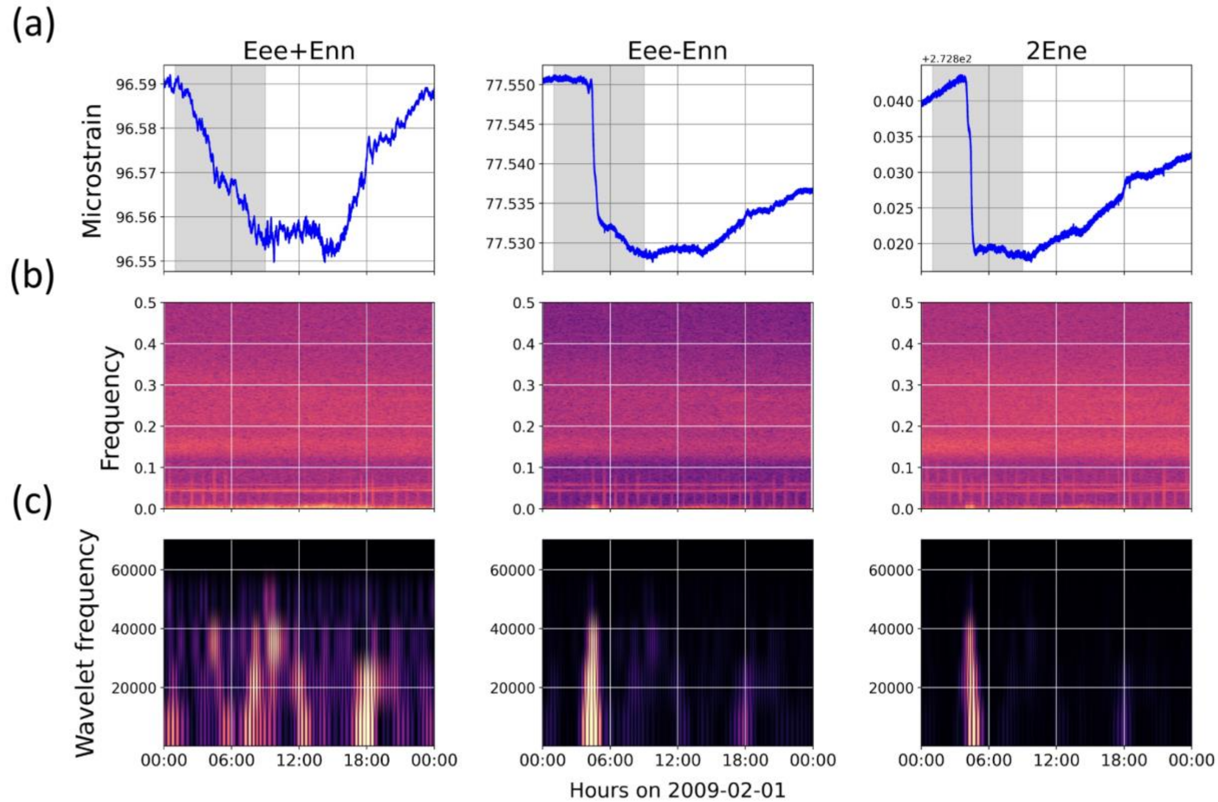

Supplementary Fig. 13: Comparison of STFT and Wavelet Transform for SSE representation. **a,** shows time series of the areal (Eee+Enn), differential (Eee−Enn), and engineering (2Een) strain components, highlighting a short-term SSE as a transient strain change (gray shaded window). **b,** displays the Short-Time Fourier Transform (STFT) spectrograms of the same components. The SSE does not produce a clear signature in the STFT domain. **c,** shows the corresponding wavelet transform spectrograms, where the SSE appears as a localized burst of energy, particularly in the lower frequency bands. The wavelet transform captures the transient nature of the event more effectively than STFT, making it a better tool for identifying SSEs.

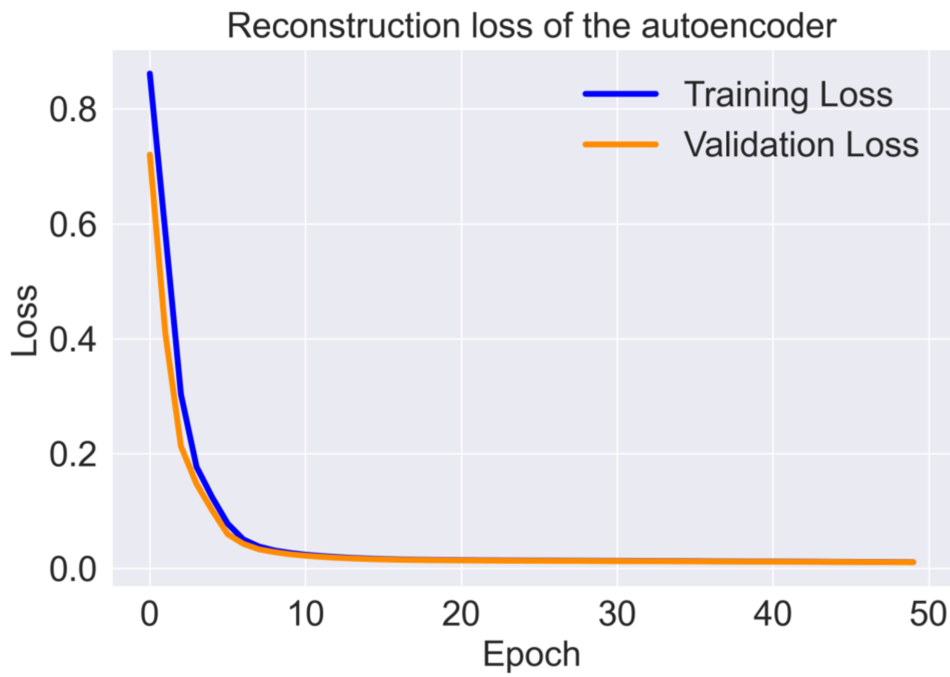

Supplementary Fig. 14: Training performance of AutoencoderZ. Reconstruction loss during training of AutoencoderZ for the B073 differential component, showing good convergence and model performance over epochs.